


## Bridging-Coupling Band Gaps in Nonlinear Acoustic Metamaterials

Xin Fang,<sup>\*</sup> Jihong Wen,<sup>†</sup> Dianlong Yu, and Jianfei Yin

Laboratory of Science and Technology on Integrated Logistics Support, National University of Defense Technology, Changsha, Hunan 410073, China

 (Received 26 May 2018; revised manuscript received 14 August 2018; published 21 November 2018)

Nonlinear acoustic metamaterials (NAMs) provide possibilities for exploiting the latest technologies for wave manipulations. Recently, the desired ultralow- and ultrabroadband wave suppressions have been achieved by chaotic bands in NAMs [Nat. Commun. **8**, 1288 (2017)]. This work describes a remote interaction mechanism in NAMs: bridging coupling of nonlinear locally resonant band gaps. Theoretical studies on a triatomic model containing two nonlinearly coupled resonances clarify the principle of bridging band gaps. Bridging band gaps greatly change the nonlinear effective mass density and generate chaotic bands between nonlinear local resonances. The bandwidth and the efficiency of the wave reduction in chaotic bands can be effectively manipulated by modulating the frequency distance between the bridging pair. NAM beams are created to experimentally demonstrate this mechanism by including the bifurcations of periodic solutions. Our study extends the knowledge of NAMs, and more nonlinear effects are anticipated based on this mechanism.

DOI: [10.1103/PhysRevApplied.10.054049](https://doi.org/10.1103/PhysRevApplied.10.054049)

### I. INTRODUCTION

Acoustic metamaterials (AMs) provide unconventional and unusual approaches for controlling subwavelength elastic/acoustic waves [1]. In 2000, a sonic crystal with embedded locally resonant (LR) objects [2] was demonstrated featuring a negative effective mass ( $m_{\text{eff}}$ ) at subwavelength scales [3]. Since then, the characteristics, underlying physics, and applications of AMs have attracted extensive attention [4]. The negative  $m_{\text{eff}}$ , negative effective bulk modulus [5] ( $E_{\text{eff}}$ ), and double-negative parameter [6–9] have been realized using the LR mechanism. LR band gaps induced by this regime suppress the low-frequency wave propagations [1]. At present, the vast majority of studies have focused on linear AMs (LAMs) [10]. In the past decade, diverse functionalities of LAMs have been explored, including sound insulation and suppression [11–13], superabsorption [14], super-resolution [15], negative refraction [16], cloaking [17,18], and phase manipulation using space-coiling metasurfaces [19,20].

However, the LR band gap is narrow in nature [10] and its generalized bandwidth  $\gamma$  (ratio of the bandwidth to its start frequency) depends on the attached mass ratio [1]. Generally,  $\gamma \ll 1$  for a single LR band gap. Moreover, the passbands of finite LAMs consist of dense resonances that amplify waves. These properties limit LAM applications in fields such as vibration and noise control, where broadband wave suppression is desired. A natural approach to expand

the total width of a band gap is connecting an LR band gap to a Bragg or other LR band gaps, that is, band-gap coupling [21,22]. The connection is feasible using multiple resonances [23,24]. The frequency distance between two band gaps is  $\Delta\omega = \omega_{\text{st}}^{(h)} - \omega_c^{(l)}$ ; herein,  $\omega_c^{(l)}$  ( $\omega_{\text{st}}^{(h)}$ ) denotes the cutoff frequency of the lower band gap (the start frequency of the higher band gap). Band gap coupling in LAMs implies  $\Delta\omega \rightarrow 0^+$  or  $\Delta\omega < 0$ , so we define it as adjacent coupling. Adjacent coupling overcomes the bandwidth of a single LR band gap to a certain extent [21–26], but the total widths are still narrow and resonances in passbands may grow.

Nonlinearities can promote the development of different methods for achieving wave manipulations. Extensive studies on nonlinear elastic-periodic structures, such as Fermi–Pasta–Ulam (FPU) chains [27,28] and granular crystals [29], have found interesting nonlinear physical phenomena, including solitons [30], amplitude-dependent band gaps [31], and acoustic diodes [29,32,33]. In weakly nonlinear electromagnetic metamaterials, many nonlinear effects such as nonlinear self-action, parametric interactions, and frequency conversion have been demonstrated [34–37]. However, nonlinear acoustic metamaterials (NAMs) are the topic of recent study. For the proposed AMs made of side holes, Helmholtz resonators, or membranes, weak nonlinearities arise when the intensity of the sound field becomes extremely high [38–40]. These nonlinear acoustic fields in AMs lead to band-gap shifting and the second-harmonic generation [41,42].

Recently, Fang *et al.* [43–45] studied the amplitude-dependent dispersion properties, bifurcations, chaos, and

<sup>\*</sup>xinfangdr@sina.com

<sup>†</sup>wenjihong@vip.sina.com

band manipulations in discrete strong NAM models. The wave in the band gap of NAMs features a multistate behavior, so the LR band gap becomes a nonlinear locally resonant (NLR) band gap [45]. The authors found that the passbands of finite NAMs become chaotic bands, in which a periodic wave becomes a chaotic emerging wave with greatly reduced wave transmission [43–45]. Furthermore, by combing the narrow band gaps and broad chaotic bands under a strongly nonlinear state, the desired ultralow frequency, ultrabroadband (double-ultra effect) and highly efficient wave suppressions were achieved in the proposed NAM beam ( $\gamma = 21$ ) and NAM plate ( $\gamma = 39$ ) [46]. The chaotic band opens new avenues for the double-ultra control of waves. However, the mechanisms giving rise to such a broad chaotic band, especially the interactions between multiple nonlinear resonances in the meta-cells [46], were not comprehensively explained. Moreover, there is great demand for innovative approaches to manipulate chaotic bands in practice. The behaviors and bifurcations of a single NLR band gap in the infinite NAM beam were reported very recently [47].

In this work, we study the influences of nonlinearly coupled resonators in periodic cells on the wave propagations in the NAMs with at least two LR band gaps. In contrast to the adjacent couplings, we find a special remote interaction between NLR band gaps, bridging coupling, that overcomes the limitation of the frequency distance  $\Delta\omega$  and enables the effective manipulation of the chaotic band. The bridging couplings of NLR band gaps give rise to a chaotic band. The bandwidth and the efficiency for wave reduction can be adjusted by the distance. Theoretical analyses of the triatomic chain clarify the principle of bridging band gaps. NAM beams are fabricated to demonstrate this mechanism by including the bifurcations of periodic solutions.

## II. PRINCIPLE OF THE BRIDGING COUPLING OF NLR BAND GAPS

A periodic triatomic chain is the fundamental model featuring the nonlinear couplings of two resonant band gaps. As shown in Fig. 1(a), the triatomic cell consists of a linear primary oscillator  $M$ - $k_0$ , and two local resonators

$m_1$ - $k_1$  and  $m_2$ - $k_2$ . The masses of the three oscillators are  $M$ ,  $m_1$ , and  $m_2$ . The stiffness of the spring connecting the primary mass  $M$  is denoted as  $k_0$ . The resonators,  $m_1$  and  $m_2$ , connect to  $M$  through the linear stiffnesses,  $k_1$  and  $k_2$ , respectively. Moreover,  $m_1$  and  $m_2$  are coupled through a linearly viscous damping  $c\dot{u}$  and an intrinsic nonlinear spring  $k_n u^3$ . In a cell, the displacements of  $M$ ,  $m_1$ , and  $m_2$  are  $x$ ,  $y$ , and  $z$ , respectively, and  $u = z - y$ .

### A. Theories of effective parameters

In the triatomic chain, the motion equations for the individual masses of the  $n$ th cell are

$$\begin{cases} M\ddot{x}_n = k_1(y_n - x_n) + k_2(u_n + y_n - x_n) + F(t), \\ m_1\ddot{y}_n = -k_1(y_n - x_n) + c\dot{u}_n + k_n u_n^3, \\ m_2(\ddot{u}_n + \ddot{y}_n) = -k_2(u_n + y_n - x_n) - c\dot{u}_n - k_n u_n^3. \end{cases} \quad (1)$$

When calculating the responses of the whole chain,  $F(t) = k_0(x_{n-1} + x_{n+1} - 2x_n)$  in Eq. (1). The effective mass,  $m_{\text{eff}}$ , describes interesting properties of acoustic metamaterials undergoing forced harmonic oscillations. To derive  $m_{\text{eff}}$ , only the motion of a single cell is necessarily considered. In this case, by specifying  $F(t) = F \cdot \sin \omega t$ ,  $x_n = X \cdot \sin \omega t$ ,  $y_n = Y \cdot \sin \omega t$ , and  $u_n = U \cdot \sin \omega t$  in Eq. (1), neglecting the damping effect and adopting the first-order harmonic-balance approach, one obtains

$$\begin{cases} -\omega^2 M X = k_1(Y - X) + k_2(U + Y - X) + F, \\ (\omega_1^2 - \omega^2)Y = \omega_1^2 X + 3k_n U^3 / (4m_1), \\ (\omega_2^2 - \omega^2)(U + Y) = \omega_2^2 X - 3k_n U^3 / (4m_2). \end{cases} \quad (2)$$

Here,  $\omega$  denotes the driving angle frequency;  $\omega_i = \sqrt{k_i/m_i}$ ,  $i = 1, 2$ , are the natural frequencies and it is specified that  $\omega_1 < \omega_2$ . With a transformation of this equation,  $X$ ,  $Y$ , and  $F$  can be expressed as functions of the variable  $U$ . The dynamic effective mass satisfies Newton's second law in the form  $F = m_{\text{eff}}(\omega)\ddot{x}$ . Then, the  $m_{\text{eff}}$  of the nonlinear triatomic cell is given by

$$m_{\text{eff}} = \frac{F}{\ddot{x}} = \frac{F}{-\omega^2 X} = \frac{k_1 \alpha_2 + k_2 \alpha_1 + M \alpha_1 \alpha_2 + \hat{k}_N U^2 [(m_1 + m_2)(k_1 + k_2) + \beta]}{\alpha_1 \alpha_2 + \hat{k}_N U^2 \beta}, \quad (3)$$

where  $\alpha_i = \omega_i^2 - \omega^2$ ,  $i = 1, 2$ ;  $\beta = M(m_1 \alpha_1 + m_2 \alpha_2)$ ;  $\hat{k}_N = 3k_n / (4m_1 m_2)$ . If  $k_n = 0$ , one obtains the effective mass of the linear triatomic cell,  $m_{\text{eff}}^{(L)}$ , as

$$m_{\text{eff}}^{(L)} = M + \frac{k_1}{\omega_1^2 - \omega^2} + \frac{k_2}{\omega_2^2 - \omega^2} \quad (4)$$

At  $\omega_1$  and  $\omega_2$ , we have

$$m_{\text{eff}}(\omega_i) = \frac{k_i}{\hat{k}_N U^2 M m_j} + \frac{(m_1 + m_2)(k_1 + k_2)}{M m_j \alpha_j} + 1 \quad (5)$$

Here, if  $i = 1, j = 2$ ; if  $i = 2, j = 1$ . Therefore, if  $\hat{k}_N U^2 \neq 0$ ,  $m_{\text{eff}}(\omega_i)$  is not infinite.

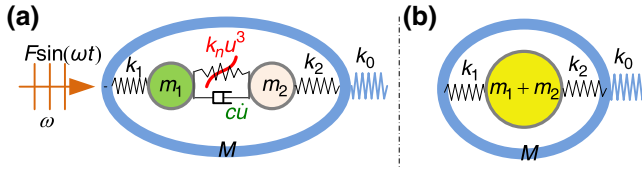


FIG. 1. (a) The triatomic cell. (b) The linear diatomic model whose inner resonator,  $m_1 + m_2$ , is coupled to  $M$  through a spring  $k_1 + k_2$ .

By repeating the process above, one obtains the linear effective mass when considering the viscous dissipation. It is expressed as

$$m_{\text{eff},d}^{(L)} = M + \frac{k_1(\omega_2^2 - \omega^2) + k_2(\omega_1^2 - \omega^2) - ic\left(\frac{k_1}{m_2} + \frac{k_2}{m_1} + \omega_1^2 - \omega_2^2\right)}{(\omega_1^2 - \omega^2)(\omega_2^2 - \omega^2) - ic\left(\frac{\omega_2^2 - \omega^2}{m_1} + \frac{\omega_1^2 - \omega^2}{m_2}\right)}. \quad (6)$$

Therefore,  $\text{Re}[m_{\text{eff},d}^{(L)}] = m_{\text{eff}}^{(L)}$ .

For the monoatomic chain consisting of the periodic oscillator  $M$ - $k_0$ , the motion equation of the  $n$ th oscillator is  $M\ddot{x}_n = k_0(x_{n-1} + x_{n+1} - 2x_n)$ . This equation describes the relation between the applied force to the cell and the acceleration of the mass center of the cell, and it can be rewritten as a difference formula, which models this chain as a continuum medium whose wave equation is given by

$$M \frac{\partial^2 x}{\partial t^2} = k_0 \frac{\partial^2 x}{\partial s^2}. \quad (7)$$

Here,  $s$  denotes the propagation direction. Under the long-wave approximation, replacing  $M$  with  $m_{\text{eff},d}^{(L)}$  leads to the wave equation of the effective continuum LAM. Then, we obtain the effective wave vector  $\kappa_{\text{eff}}$  of this LAM,

$$\kappa_{\text{eff}} = \omega \sqrt{m_{\text{eff},d}^{(L)} / k_0} \quad (8)$$

The imaginary part of  $\kappa_{\text{eff}}$ ,  $\text{Im}(\kappa_{\text{eff}})$ , approximately shows the dissipative characteristic of the effective LAM. A larger  $\text{Im}(\kappa_{\text{eff}})$  leads to a stronger attenuation of the wave.

Moreover, if the stiffness between  $m_1$  and  $m_2$  approaches infinity, they behave as single resonator whose mass and stiffness are  $m_1 + m_2$  and  $k_1 + k_2$ , respectively. In this limit case (Lc), the triatomic model becomes the diatomic model shown in Fig. 1(b). The motion equation of the  $n$ th cell in this diatomic model is

$$\begin{cases} M\ddot{x}_n + (m_1 + m_2)\ddot{v}_n = F(t), \\ \ddot{v}_n = -\omega_{Lc1}^2(v_n - x_n), \end{cases} \quad (9)$$

where the natural frequency  $\omega_{Lc1} = \sqrt{(k_1 + k_2)/(m_1 + m_2)}$ , and  $F(t) = k_0(x_{n-1} + x_{n+1} - 2x_n)$ . Similar with Eq. (1),

when considering the property of the local resonance, the steady response of  $M$  driven by  $F(t) = F \sin \omega t$  is

$$X = \frac{F \cdot (\omega_{Lc1}^2 - \omega^2)}{-\omega^2 M (\omega_{Lc2}^2 - \omega^2)}, \quad \omega_{Lc2} = \omega_{Lc1} \sqrt{1 + \frac{m_1 + m_2}{M}}. \quad (10)$$

Therefore, the steady response features a peak at the frequency  $\omega_{Lc2}$  when a force is specified. This limit case helps explain the properties of the nonlinear triatomic model.

## B. Properties of the effective mass

To study the properties of the effective mass  $m_{\text{eff}}/M$  and the responses of the finite chain, we specify the parameters  $M = 1$ ,  $m_1 = 0.3$ ,  $m_2 = 0.3$ ,  $\omega_0 = (k_0/M)^{1/2} = 6$ , and  $\omega_1 = 2$ . The distance between two band gaps is controlled by  $\omega_2$ .  $\omega_2 = 4$  and  $\omega_2 = 8$  are taken as examples. In this case,  $\omega_{Lc2} \approx \omega_2$ . As illustrated in Figs. 2 and 3, two narrow bands of negative  $m_{\text{eff}}/M$  are generated near the resonant frequencies  $\omega_1$  and  $\omega_2$  in LAMs. This regime results in two LR band gaps, LR1 and LR2.

Equation (3) implies that the  $m_{\text{eff}}$  of a NAM relates to the quadratic term of the relative displacement,  $U^2$ . Therefore, the  $m_{\text{eff}}/M$  near a resonant frequency, as indicated by Eq. (5), depends on the motion of the other resonator. The phase of  $U$  does not affect  $m_{\text{eff}}$ . There are two different ways to calculate  $m_{\text{eff}}$  with Eq. (2): specifying (i) the input force,  $F$ , or (ii) the displacement,  $X$ . In the analyses below,  $S^{(F)}$  or  $S^{(X)}$  denotes the symbol  $S$  in case (i) or (ii), respectively. Values of  $m_{\text{eff}}^{(L)}$  in the two cases are identical. However,  $m_{\text{eff}}$  of the nonlinear model features different behaviors for the two cases.

As shown in Figs. 2(a) and 2(c), the curve of a nonlinear resonance consists of three branches, branches 1, 2 and 3, in which branches 2 and 3 are connected by a saddle-node bifurcation  $\omega_{Ji}$ ,  $i = 1, 2$ .  $\omega_1 < \omega_{J1} < \omega_2$ .  $\omega_{J1}$  and  $\omega_{J2}$  depend on each other attributing to the coupling of the two resonances. As is well known, branch 2 corresponds to unstable solutions, thus its effects are negligible. As clarified recently [47],  $\omega_{Ji}$  greatly influences the wave propagation in NAMs.

The first nonlinear resonance characterizes a peak at  $\omega_p^{(F)}$  or  $\omega_p^{(X)}$ , where  $U \rightarrow \infty$ . Analyses indicate that  $\omega_p^{(F)} = \omega_{Lc2}$  and  $\omega_p^{(X)} = \omega_{Lc1}$ , demonstrating that the triatomic model acts as a diatomic model [see Fig. 1(b)] at  $\omega_p$  if  $U$  is large: here,  $m_1$  and  $m_2$  behave as a single resonator although they are separated in space. This property shows there are strong couplings between  $m_1$  and  $m_2$  on branch 1 of the first nonlinear resonances. Their mass and stiffness are shared through this interaction, and this coupling enables the energy transfer.

A branch of  $m_{\text{eff}}$  matches the corresponding branch of the nonlinear resonances (see Fig. 2), so the bifurcation

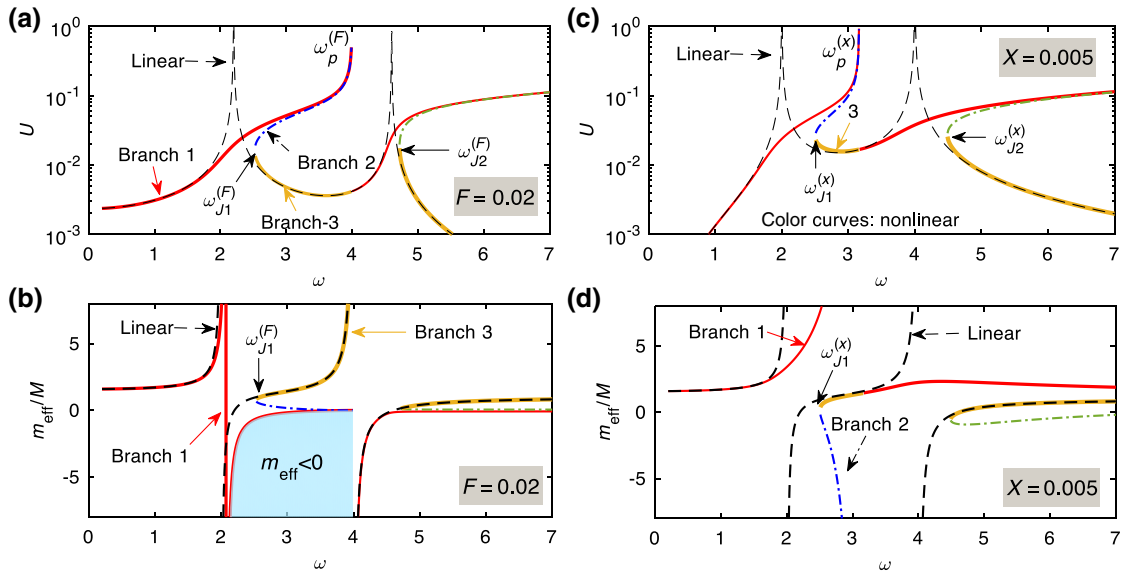


FIG. 2. (a),(c) Resonant curves of  $U$  and (b),(d) the corresponding effective mass  $m_{\text{eff}}/M$  of the triatomic model.  $\omega_2 = 4$ . (a),(b) Solved by specifying  $F = 0.02$ ; (c),(d) solved by specifying  $X = 0.005$  in Eq. (2). The dashed black curves represent linear results. The colored curves are the nonlinear results for  $k_n = 500k_1$ , in which the dash-dot curves denote branch 2 (unstable solutions).

point of  $m_{\text{eff}}$  is still  $\omega_{ji}$ . Strong couplings between the nonlinear resonances give rise to the strong couplings of NLR band gaps. Branch-3 of a nonlinear resonance nearly coincides with the linear results, as does  $m_{\text{eff}}$ .  $\omega_{\infty i}$  symbolizes the frequency for  $m_{\text{eff}} \rightarrow -\infty$ ,  $i = 1, 2$ . For LAMs, Eq. (4) indicates  $\omega_{\infty i} = \omega_i$ .

When the force,  $F$ , is specified [see Figs. 2(a) and 2(b)], the band for  $m_{\text{eff}}/M < 0$  in the LAM relates to the left part of a resonant peak, and the deformation of this part becomes branch 1 of a nonlinear resonance. Thus, the band

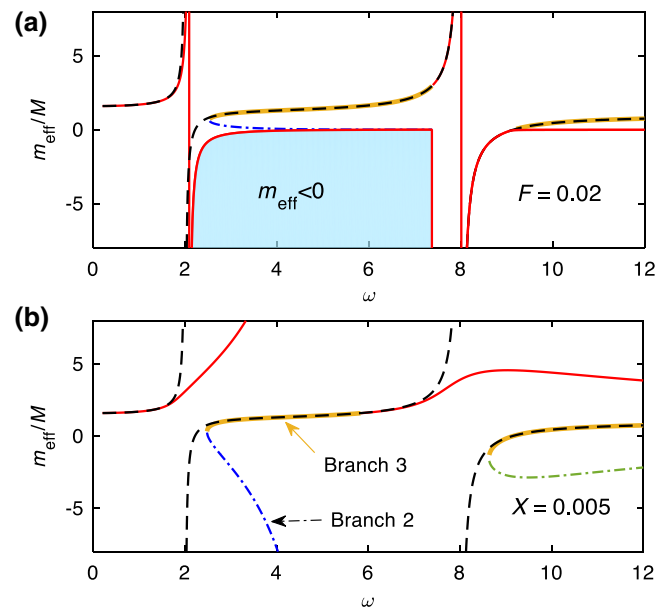


FIG. 3. Effective mass  $m_{\text{eff}}/M$  of the triatomic model by specifying (a)  $F = 0.02$  and (b)  $X = 0.005$  for the case  $\omega_2 = 8$ .

for the negative  $m_{\text{eff}}/M$  in the NAM originates from branch 1. Moreover, there are still two bands for  $m_{\text{eff}}/M < 0$  near  $\omega_1$  and  $\omega_2$  in the NAM model. However, the nonlinearity shifts the first negative  $m_{\text{eff}}/M$  band near  $\omega_{\infty 1}$  to higher frequencies, and a stronger nonlinearity brings a larger deviation to  $\omega_1$ . As is well established, this is also the process by which LR1 becomes the NLR band gap, NLR1, in this NAM model [45]. LR2 will also become NLR2 when the giant nonlinearity appears. On branch 1,  $m_{\text{eff}}$  monotonically approaches 0 at  $\omega_p^{(F)} = \omega_{Lc2}$ . Accordingly,  $m_{\text{eff}}/M < 0$  in the interval  $(\omega_{\infty 1}, \omega_{Lc2})$ . Thus, branch 1 greatly expands the first negative mass region and connects the two negative mass bands, indicating that the nonlinear coupling between the two resonators  $m_1$  and  $m_2$  shares the negative  $m_{\text{eff}}$  between NLR1 and NLR2 through the energy transmission.

In contrast, when specifying  $X$  in Eq. (2), solving  $U$  and  $Y$  becomes a two-degrees-of-freedom problem where  $F$  acts as the boundary condition. In this case [see Figs. 2(c) and 2(d)], the linear resonances peak at  $\omega_i$ , and  $m_{\text{eff}}/M < 0$  corresponds to the right part of the resonances. For the NAM,  $m_{\text{eff}}$  is always positive on branch 1, and the negative  $m_{\text{eff}}$  depends on branch 3.  $\omega_j^{(x)}$  initiates a near-field NLR gap (if it exists) in the NAM [47]. As  $\omega_j^{(x)} > \omega_i$ , the NLR gaps arising from the negative  $m_{\text{eff}}$  become narrower and disappear in conditions of strong nonlinearities. However, between the two resonances,  $m_{\text{eff}}(\omega_p^{(x)}) \rightarrow +\infty$  for branch 1,  $m_{\text{eff}}(\omega_p^{(x)}) \rightarrow -\infty$  for branch 2, and  $\omega_p^{(x)} = \omega_{Lc1} \ll \omega_2$ , which is different from the linear case and the nonlinear properties above  $\omega_2$ .

Therefore, both cases show that the nonlinear coupling of two local resonators greatly changes the properties of

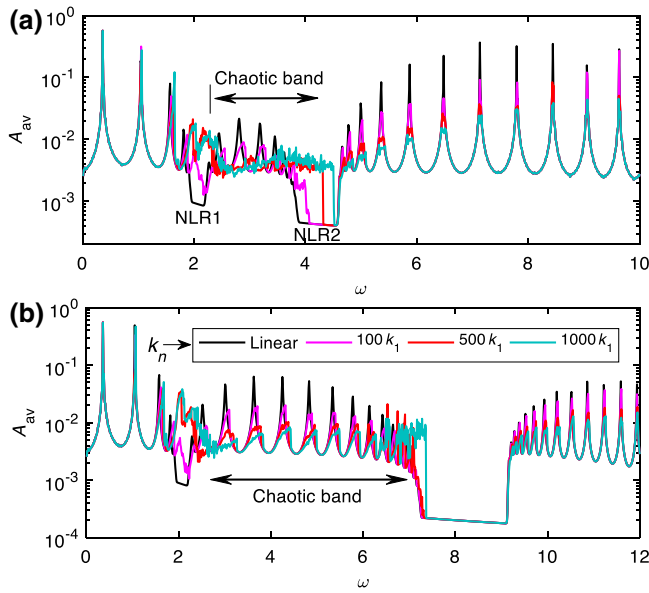


FIG. 4. Responses of the finite chain composed of 20 cells. (a)  $\omega_2 = 4$ ; (b)  $\omega_2 = 8$ . The legend of (a) is identical to (b).

$m_{\text{eff}}$  and thus influences the wave propagation in NAMs. As illustrated in Fig. 3, the frequency distance,  $\Delta\omega$ , between the two resonances has little effect on the coupling between NLR1 and NLR2. Therefore, this interaction is independent of  $\Delta\omega$  in theory, indicating that it works in the situation with a remote frequency distance. Its properties are essentially different from those of the adjacent coupling.

### C. Responses of the finite chain

A finite chain made of 20 (or 12) cells is adopted to describe the response properties. The left boundary (the driving displacement) of the chain is  $x_0 = A_0 \sin \omega t$ , and the right is free. To make the comparison more rigorous, a dissipation  $c = 0.01$  is considered. The numerical integration method is employed to directly solve the responses. The integration time is 1000 s.  $A_{\text{av}}(\omega)$  denotes the average displacement of the last oscillator  $M$  in 800–1000 s (steady response). By specifying  $A_0 = 0.005$ , the nonlinear strength is modulated by the coefficient  $k_n$ . Here,  $A_0$  is equal to  $X$ , as specified in Eq. (2).

As shown in Fig. 4, the passbands of a finite LAM consist of dense resonances, although their amplitudes are limited by the damping. In the case  $\omega_2 = 4$ , the maximum amplitude in the second passband is smaller than that in the first and the third passbands. For the given parameters,  $k_n = 100k_1$ ,  $500k_1$ , and  $1000k_1$  simulate the weak, moderate, and moderate (but stronger) nonlinearities, respectively. In contrast with the linear case, weak nonlinearity can reduce  $A_{\text{av}}$  at the resonances in the second passband and the lower part of the third passband. Enhancing the nonlinear strength leads to larger amplitude reductions and a broader reduction band. Moreover,

$k_n = 500k_1$  makes NLR1 and the lower part of NLR2 close when  $\omega_2 = 4$ , which agrees with the laws illustrated in Fig. 2(d). Waves inside the NLR band gaps are relevant to the bifurcations of the fundamental waves and the high-order harmonics [47]. The frequency range in which the resonances are suppressed is the chaotic band. If other parameters are constant, increasing  $\omega_2$  to  $\omega_2 = 8$  broadens the second passbands and the LR2. The interesting phenomenon is that the chaotic band is also expanded under the same nonlinear strength. Moreover, at the resonances in the chaotic band, further strengthening  $k_n$  to  $1000k_1$  results in larger reductions of  $A_{\text{av}}$  for  $\omega_2 = 8$ , but it has little influence on  $A_{\text{av}}$  for  $\omega_2 = 4$ , as  $500k_1$  has already attenuated the value greatly.

Let us define  $A_{2,\text{max}} = \max[A_{\text{av}}(\omega)]$  in the second passband  $\omega \in (\omega_c^{(1)}, \omega_{\text{st}}^{(2)})$ , where  $\omega_c^{(1)}$  is the cutoff frequency of NLR1 and  $\omega_{\text{st}}^{(2)}$  denotes the start frequency of NLR2. Here, “ $\max(\cdot)$ ” is a function for the maximum value. Similarly,  $A_{3,\text{max}} = \max[A_{\text{av}}(\omega)]$  for  $\omega > \omega_c^{(2)}$ . Therefore,  $G = A_{2,\text{max}}^L / A_{2,\text{max}}^N$  indicates the influences of the nonlinearity on the responses in the second passband, where the superscripts  $L$  and  $N$  correspond to the linear and nonlinear cases, respectively. If  $G > 1$ , a larger  $G$  indicates a higher efficiency for wave attenuation. As shown in Fig. 5(a), when modulating  $\omega_2$  in  $3 < \omega_2 < 9$  under moderate nonlinearity,  $k_n = 500k_1$ , we have  $A_{2,\text{max}}^L \propto \Delta\omega$  and  $A_{3,\text{max}}^L \propto 1/\Delta\omega$ , where  $\Delta\omega = \omega_2 - \omega_1$ . This principle reveals that the dissipative effect of LAMs can also be modulated by  $\Delta\omega$ .  $\text{Im}(\kappa_{\text{eff}})$ , evaluated from Eq. (8), demonstrates this feature. As indicated by Fig. 6,  $\text{Im}(\kappa_{\text{eff}}) \gg c = 0.01$  inside the band gaps; as  $\Delta\omega$  increases,  $\text{Im}(\kappa_{\text{eff}})$  in the second passband decreases, but  $\text{Im}(\kappa_{\text{eff}})$  in the third passband increases. The dissipative effects of the linear resonances follow the same regular trend as  $\text{Im}(\kappa_{\text{eff}})$ , leading to the behaviors of  $A_{2,\text{max}}^L$  and  $A_{3,\text{max}}^L$  characterized in Fig. 5(a). Moreover, the width of LR2 also increases with  $\Delta\omega$ .

For the NAM model, on the whole,  $A_{2,\text{max}}^N \propto \Delta\omega$  and  $A_{3,\text{max}}^N \propto 1/\Delta\omega$ . However, due to the chaotic band effect,  $A_{j,\text{max}}^N < A_{j,\text{max}}^L$ ,  $j = 2, 3$ , and  $A_{2,\text{max}}^N$  increases more slowly than does  $A_{2,\text{max}}^L$  with  $\Delta\omega$ . Accordingly, when  $\omega_2$  increases from 3 to 7.5, the efficiency  $G$  increases from 1.48 to 5.75 for the chain composed of 20 cells, as shown in Fig. 5(b). However,  $G$  obviously decreases if we further increase  $\omega_2$  to  $\omega_2 > 8$  attributing to the amplified responses near NLR2 [see Fig. 4(b)]; the NAM remains  $G \approx 5$  if this effect is neglected. Moreover,  $G$  for  $k_n = 1000k_1$  is approximately equal to that in the case  $k_n = 500k_1$ . These principles indicate that increasing the distance between two NLR band gaps to a certain extent can broaden the chaotic band and enhance its efficiency to suppress the resonances. Further increasing the nonlinear strength provides higher suppressing efficiencies [43–46]. With the combination of the features in the second and the third passbands with the width of NLR2, the total bandwidth for wave

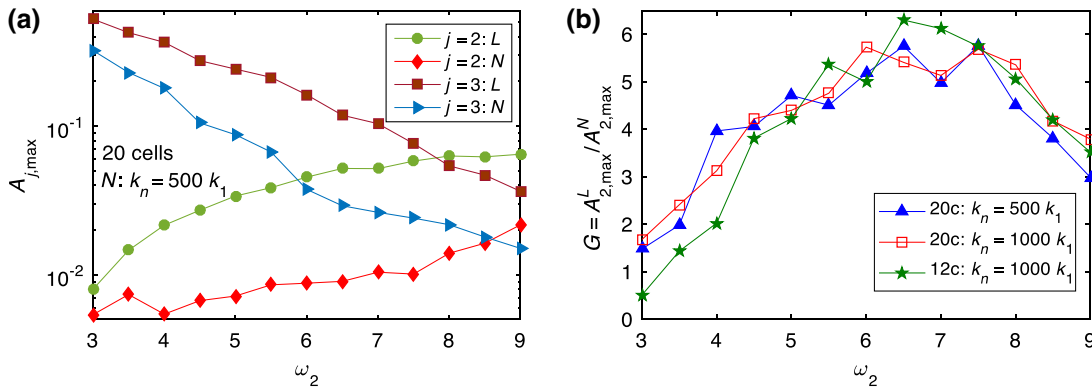


FIG. 5. Response amplitudes of the finite triatomic chain.  $A_0 = 0.005$ . (a)  $A_{2,\max}$  and  $A_{3,\max}$  in linear (“L”) and nonlinear ( $N$ :  $k_n = 500k_1$ ) cases. (b) The ratio  $A_{2,\max}^L/A_{2,\max}^N$  for chains composed of 20 cells (20c) and 12 cells (12c), respectively.

attenuation and suppression is significantly expanded by increasing  $\Delta\omega$ . It is noteworthy that these chaotic band effects manipulated by the distance of NLR band gaps depend little on the damping, though the damping can also attenuate the wave. This type of interaction between band gaps arises from the nonlinear effect in nature. In addition, for the chain with 12 cells [see Fig. 5(b)], the trend of the curve  $G-\omega_2$  is consistent with that for the chain composed of 20 cells. The  $\max[G^{(12c)}]$  at  $\omega_2 = 6.5$  even reaches 6.3 and  $\max[G^{(12c)}] > \max[G^{(20c)}]$ , although  $G^{(12c)} < G^{(20c)}$  for  $\omega_2 \leq 4$ ; herein, the superscript “nc” denotes the number of cells. Therefore, the regularity depends weakly on the length of the finite chain.

When a finite NAM has two or more NLR band gaps, the analyses above clearly demonstrate that these band gaps exhibit remote ( $\Delta\omega \gg 0$ ) couplings by generating the chaotic band together to significantly suppress the resonances; increasing  $\Delta\omega$  to a certain extent under a finite nonlinear strength promotes the suppression efficiency and bandwidth. Moreover, the size of the NAM does not notably change these laws. In this coupling, the band gaps behave as bridge piers, and the chaotic band acts as the bridge floors supported by piers, so we refer to this situation as bridging coupling. Two coupled-NLR band gaps are a bridging pair. Bridging coupling is essentially

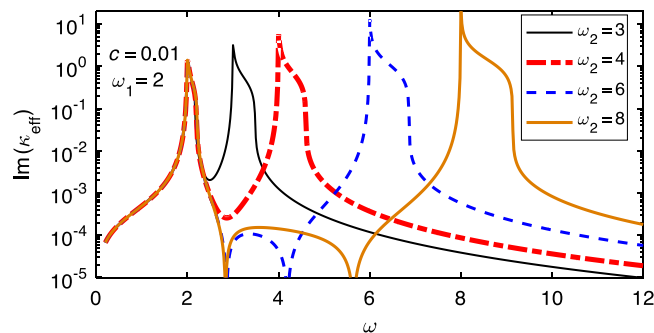


FIG. 6. The imaginary part of the wave vector  $\text{Im}(\kappa_{\text{eff}})$  of the linear triatomic model under damping case.  $\omega_1 = 2$ ,  $c = 0.01$ .

different from the adjacent couplings. Because the nonlinear strength, particularly the coefficient  $k_n$ , realized in a real structure is generally limited by the scale, the amplitude, and manufacturing technologies, it is of paramount importance to use bridging couplings to manipulate the chaotic band effect in practice.

### III. VERIFICATION OF THE BRIDGING COUPLING OF NLR BAND GAPS

#### A. Metamaterial design

To verify the bridging coupling of NLR band gaps, we fabricated NAM beams made of periodic cells, as shown in

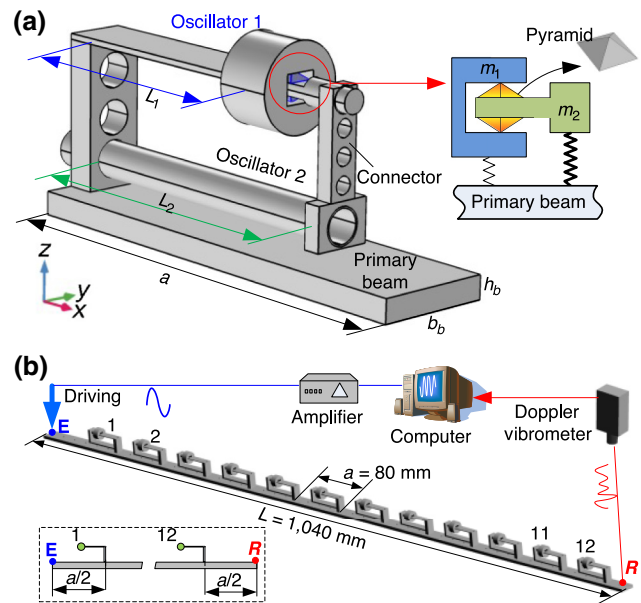


FIG. 7. Structure of the NAM beam. (a) Structure of a cell; the right schematic is the supposed equivalent model. (b) Structure of the NAM beam consisting of 12 cells and its measuring method. Points E and R are the driving and measuring points, respectively. Their positions are labeled in the box.

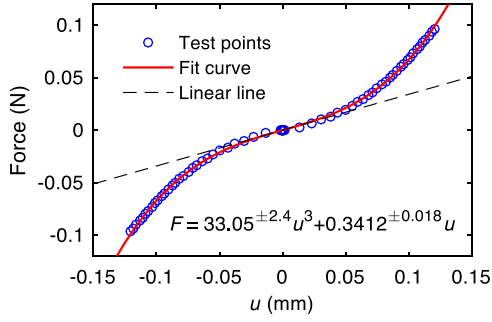


FIG. 8. Nonlinear relations between the compression force  $F$  and the deformation  $u$  of a pair of rubber pyramids.

Fig. 7(a). The primary structure is a uniform linear beam and the lattice constant  $a = 80$  mm. Two oscillators are fixed on the primary beam through a stiff strut. Oscillator 1 consists of a cantilever thin beam and a tip mass  $m_1$ . Oscillator 2 consists of a cantilever tube (or a thick beam) and a connector (acting as mass  $m_2$ ) fixed at the end of the tube (or the beam). The first resonant frequency of oscillator 2 is designed to be higher than that of oscillator 1. There is a square hole in  $m_1$ . A pair of small rubber pyramids is attached to the connector and both of them are put in the square hole. The rubber pyramids are undeformed at rest. In theory, the clearance between the peak of the rubber and the wall of the hole is zero. The relative motion of the two oscillators will compress the pyramid rubble. With a high-precision instrument, DMA Q800 (made by TA Instruments), we measure the force,  $F$ , generated by a pyramid rubber with the compression deformation,  $u$ , in the quasistatic compression experiments at about 30 °C.

As depicted in Fig. 8, the relationship  $F$ - $u$  induced by a pair of rubber pyramids can be fit with a cubic nonlinear function,  $F(u)$ , accurately, as

$$F(u) = k_0 u + k_n u^3. \quad (11)$$

We realize that  $k_n = \beta \times 10^{10}$  N/m<sup>3</sup> and  $\beta = 1 \sim 4$  in experiments. In theoretical analyses, we specify  $k_n = 1 \times 10^{10}$  N/m<sup>3</sup>. This  $k_n$  enables us to achieve moderate nonlinearities with finite driving amplitudes. The linear

stiffness  $k_0$  of the rubber is negligible compared with the stiffnesses of the oscillators.

The whole metamaterial beam consists of 12 cells, as shown in Fig. 7(b). The total length of the beam is 1040 mm. In experiments, different levels of broadband white-noise signals drive the beam at point  $E$ . A laser Doppler vibrometer measures the responses at the right end,  $R$ . The driving levels are modulated by the voltage of the amplifier. We fabricated NAM1 and NAM2 to study the influence of frequency distance on the wave transmission of NAMS. The first eigenfrequency of oscillator 2 in NAM2 is higher than that of NAM1. NAM1 is shown in Fig. 7(b). NAM2 consists of the periodic cells shown in Fig. 7(a). Their primary beams are the same, and the width, thickness, density, and modulus of the beams are  $b_b = 20$  mm,  $h_b = 4$  mm,  $\rho = 2700$  kg/m<sup>3</sup>, and  $E = 70$  GPa, respectively. The concentrated mass and inertia at the fixed point in a cell are  $m_0 = 3$  g and  $J_0 = 0$ , respectively. Parameters of oscillators 1 and 2 are listed in Table I. Their definitions are  $\rho_i$  is density,  $E_i$  is modulus,  $A_i$  is section area,  $I_i$  is inertia moment,  $L_i$  is length,  $m_{ii}$  is tip mass, and  $J_{ii}$  is tip inertia; herein, the subscript  $i = 1, 2$  denotes parameters relevant to oscillator 1 or oscillator 2, respectively. In Fig. 7(a), inverting the connector on oscillator 2 decouples oscillator 1 and oscillator 2. In this situation, they become the typical linear metamaterials, LAM1 and LAM2, with multiple local resonances.

## B. Dispersion and transmission properties

By considering the first and second flexural modes of oscillator 1, and the first flexural mode of oscillator 2, this manuscript establishes physical models of oscillators 1 and 2 with the mode superposition method (see Appendix). Then, the finite element (FE) model of a periodic cell is built based on the Bloch theorem [46]. The harmonic balance method is adopted to solve the dispersion curves of this model [46]. As illustrated in Fig. 9, LAM1 and LAM2 have four band gaps below 1400 Hz. Their ranges are listed in Table II. LR1 and LR3 are induced by the first and the second flexural modes of oscillator 1, respectively. LR2 is generated by the first flexural mode of oscillator 2. Both LAM1 and LAM2 have Bragg band gaps

TABLE I. Parameters of oscillator 1 and 2 in NAM1 and NAM2. The subscript  $i = 1, 2$ .

Symbol	Oscillator 1		Oscillator 2	
	NAM1	NAM2	NAM1	NAM2
$\rho_i$ (kg/m <sup>3</sup> )	2700	2700	2700	7800
$E_i$ (GPa)	70	70	70	200
$A_i$ (m <sup>2</sup> )	$8 \times 10^{-6}$	$1 \times 10^{-5}$	$1.6 \times 10^{-5}$	$5.37 \times 10^{-6}$
$I_i$ (m <sup>4</sup> )	$4.27 \times 10^{-13}$	$8.33 \times 10^{-13}$	$3.41 \times 10^{-12}$	$1.75 \times 10^{-11}$
$L_i$ (mm)	32	44.3	43.5	59.5
$m_{ii}$ (g)	11.45	11.45	2.2256	4.5
$J_{ii}$ (kg m <sup>2</sup> )	$2.56 \times 10^{-7}$	$2.05 \times 10^{-7}$	$1.8 \times 10^{-7}$	$5.25 \times 10^{-7}$

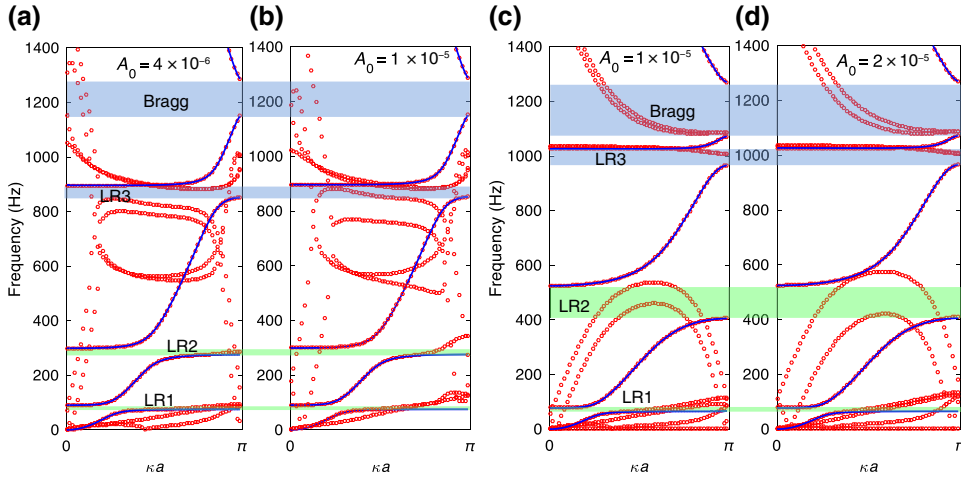


FIG. 9. Dispersion curves of linear and nonlinear metamaterials for different amplitudes. (a),(b) NAM1; (c),(d) NAM2. Different wave amplitudes,  $A_0$ , are labeled on the panels. The solid blue curves are linear dispersion results, and all the red points are nonlinear dispersion results. The wave vector  $0 < \kappa < \pi/a$ . The shaded bands are linear band gaps.

near 1200 Hz. The generalized bandwidth of a band is  $\gamma = (f_{\text{cut}} - f_{\text{st}})/f_{\text{st}}$ , where  $f_{\text{st}}$  ( $f_{\text{cut}}$ ) denotes the start (cutoff) frequency. LAM2-LR2 has the largest  $\gamma$  ( $\gamma = 0.295$ ); however,  $\gamma \ll 1$ . Therefore, those band gaps are narrow. The main difference between LAM1 and LAM2 lies in the position of LR2: the distance between LR1 and LR2 in LAM2 is greater.

The transfer function is  $H(\omega) = 20 \log_{10}[X_R(\omega)/X_E(\omega)]$  dB, where  $X_i(\omega)$  is the frequency spectrum at point  $i$ . The  $H(\omega)$  of NAM1 and NAM2 at different excitation levels are shown in Fig. 10. The band gaps, LR1, LR2, and LR3, presented by  $H(\omega)$  of the linear-decoupled cases agree well with the dispersion curves. The dispersion solutions of NAMs depend on the wave amplitude,  $A_0$  [43–46]. To provide the values of  $A_0$  that are consistent with the experiments, the average excitation displacements in 50–100 Hz (near LR1) are adopted as references for  $A_0$ .  $A_0$  also indicates different driving levels. Therefore, we use  $A_0 = 4 \mu\text{m}$  and  $10 \mu\text{m}$  for NAM1, and use  $A_0 = 10 \mu\text{m}$  and  $20 \mu\text{m}$  for NAM2. The smaller  $A_0$  approximates the experimental input wave. In addition to the five dispersion curves identical to those of the relevant LAMs, NAMs have multiple dispersion solutions that will bifurcate (see Fig. 9). Most of these multiple solutions have large imaginary parts, leading to rapid attenuations of the waves. For band gaps, the nonlinearity first shifts the lower boundary of LR1 upward; further enhancing the nonlinear strength can also shift the lower boundary of LR2. However, their upper boundaries remain almost constant, so that LR1 closes first. In this process, LR band gaps become NLR gaps. These regimes are consistent with the regularities shown by the triatomic model in Fig. 2. A much stronger nonlinearity is required

to shift LR2 of NAM2 due to its higher frequency. This situation is similar for LR3.

As shown in Fig. 10, for LAMs, the transmission in the band gaps is reduced by 30 dB. However, the passbands consist of dense resonances that amplify waves more

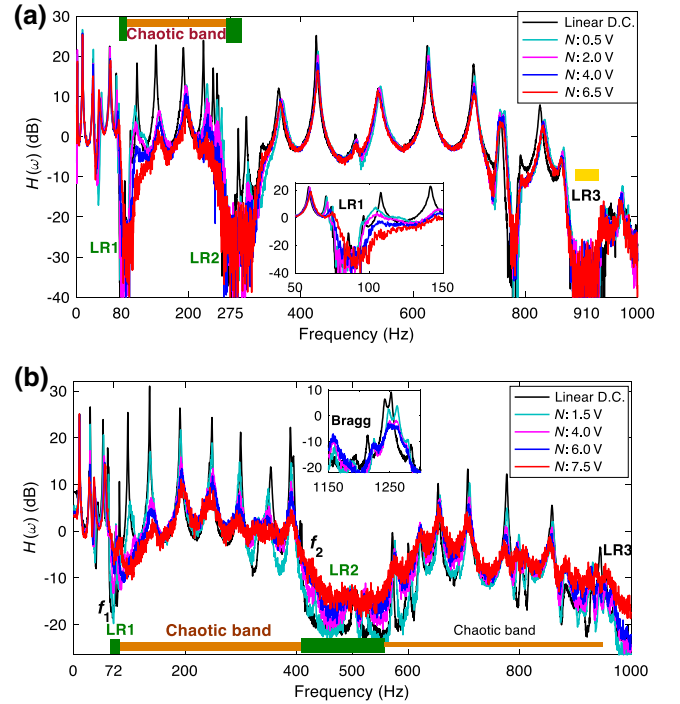


FIG. 10. Transfer function  $H(\omega)$  for different excitation levels. (a) NAM1. (b) NAM2. The shaded frequency ranges represent band gaps and chaotic bands. The average amplitude in 50–100 Hz (near LR1) is used to evaluate different excitation levels. NAM1: {0.5 V, 0.7446  $\mu\text{m}$ }, {2.0 V, 2.7458  $\mu\text{m}$ }, {4.0 V, 5.4454  $\mu\text{m}$ }, and {6.5 V, 8.7768  $\mu\text{m}$ }; NAM2: {1.5 V, 0.8734  $\mu\text{m}$ }, {4.0 V, 2.372  $\mu\text{m}$ }, {6.0 V, 3.502  $\mu\text{m}$ }, and {7.5 V, 11.7  $\mu\text{m}$ }. Linear D.C. in legends represents the decoupled case, which is the linear state of the metamaterial. N-xV denotes the voltage of the amplifier used to drive the NAM.

TABLE II. Ranges of band gaps in LAM1 and LAM2.

	LR1 (Hz)	LR2 (Hz)	LR3 (Hz)	Bragg (Hz)
LAM1	75.2–90.8	275.8–299.3	851.9–896.1	1151–1286
LAM2	64.5–77.9	405.2–524.6	965.9–1027	1072–1270



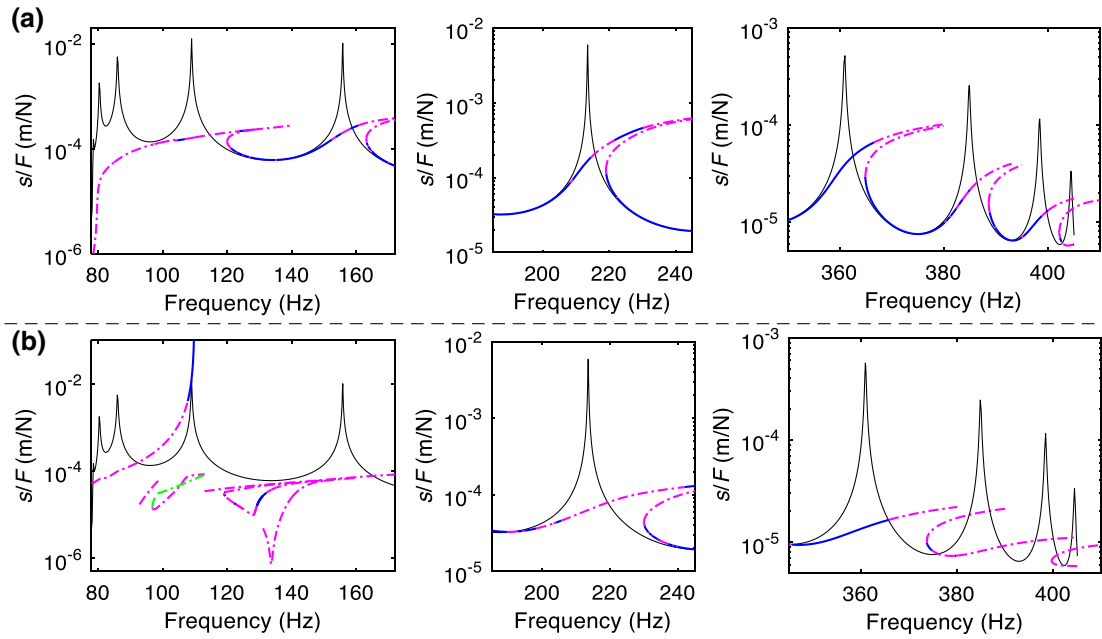


FIG. 11. Bifurcations of periodic solutions found by the perturbation continuation approach. (a)  $F = 1$  N; (b)  $F = 5$  N. All the solutions are convergent. The solid black curves are solutions of LAM2; the solid blue (dashed magenta/green) curves represent stable (unstable) periodic solutions of NAM2.

than 20 dB. As characterized by  $H(\omega)$  of NAM1 [see Fig. 10(a)], increasing the driving amplitude shifts LR1 to higher frequencies, which is consistent with the dispersion curves. Moreover, wave transmissions at the resonances in the second passbands (LR1-LR2) decrease by 15–30 dB when a strong nonlinearity appears (6.5 V). As clarified [46], such significant wave attenuation is induced by the chaotic band effect because the second passband becomes a chaotic band. However, in the third passband, only the resonances near LR2 are suppressed, and the maximum values of  $H(\omega)$  in NAM1 (for 6.5 V) and LAM1 reach 16 and 25 dB, respectively. As a result, the wave attenuations of NAM1 in the strongly nonlinear regime mainly appear in the 70–300 Hz range that consists of the chaotic band and band gaps; its generalized width  $\gamma > 3.3$ . Those features of NAM1 are consistent with the phenomena shown in the short-frequency distance case of the triatomic model [see Figs. 4(a) and 4(c)], which verifies that the wave attenuations in the chaotic band are controlled by the bridging-coupling pair NLR1-NLR2. The energy transfer between oscillator 1 and oscillator 2 alters the negative mass properties and generates the chaotic band to suppress the nonlinear resonances. In theory, there are bridging couplings between NLR3 and other band gaps. However, a much stronger nonlinearity is required to generate obvious interactions because of the long-frequency distances.

When the distance between NLR1 and NLR2 increases, as predicted by the remote bridging couplings of the triatomic model, the chaotic band suppressing nonlinear resonances becomes broader with the second passband; the

maximum  $H(\omega)$  of LAM in the third passband decreases; and the third passband of NAM can also suppress the resonances. As shown in Fig. 10(b), the  $H(\omega)$  of NAM2 features the same properties as the predictions above: in the second passband (the chaotic band), the resonant transmissions in the strongly nonlinear state (7.5 V) decrease by 15–35 dB relative to those in the decoupled linear state; NLR1 is closed and shifted upward; the maximum values of the  $H(\omega)$  of NAM2 under 6.0 V and LAM2 are just 6 and 13 dB, which are much lower than those of NAM1. Therefore, NLR1 and NLR2 of NAM2 are bridging coupled. Moreover, different from the properties of the third passband of NAM1, resonances far from NLR2 and near NLR3 in NAM2 are also suppressed. This effect even spreads to the resonances (near 1250 Hz) above the Bragg band gap [see the small panel in Fig. 10(b)]. Some of this suppression arises from the farther bridging pair NLR1-NLR2 in the strongly nonlinear state, but the bridging coupling between NLR2 and NLR3 also has an effect. Therefore, the bridging couplings between multiple NLR band gaps are desirable. Even if neglecting the Bragg band gap and higher frequencies, those bridging couplings in NAM2 bring wave suppressions/attenuations in an ultralow frequency and ultrabroadband of 60–1000 Hz. The generalized bandwidth reaches  $\gamma > 15.6$ , which is approximately five times broader than that of NAM1. Experimental phenomena demonstrate that increasing the distance between bridging NLR band gaps can manipulate the vibration suppression bandwidth and efficiency in their common chaotic band.

### C. Bifurcations of periodic solutions

To confirm that the responses at the nonlinear resonances are chaotic, we find periodic solutions of the NAM2 FE model by combining the harmonic average method and the perturbation continuation approach. The stability of a periodic solution is determined by the eigenvalues of the Jacobian matrix. A driving force,  $F$ , is applied at point  $E$ . Dissipations of the rubber pyramids and the structural damping are taken into consideration. These approaches are detailed in the Appendix.

We find periodic solutions in three typical ranges in the second passband: the lower (near LR1, 80–170 Hz), the middle (210–245 Hz), and the upper (near LR2, 350–410 Hz) parts, as shown in Fig. 11. Under  $F = 1$  N, the nonlinear resonances characterize three branches bending right, but all the resonant peaks are unstable (or the stable and unstable ranges appear alternately), and their amplitudes are much smaller than those of the linear resonant peaks. In this situation, the root branches of the nonlinear resonances are stable and coincide with the linear results, which indicate quasiperiodic solutions. These phenomena are similar to the studies on diatomic/tetatomic models in Ref. [45]. Moreover, at the lower and the upper parts near the band gaps, all solutions become unstable, indicating that nonlinear effects are present in both oscillator 1 and oscillator 2.

Upon further increases in the driving force to  $F = 5$  N [Fig. 11(b)], not only the resonant peaks but also their roots become unstable; the unstable ranges enlarge, and solutions of the middle part become unstable. For example, in 80–170 Hz under  $F = 5$  N, stable solutions can only be found in some narrow frequency intervals; other ranges consist of complex bifurcation branches formed by unstable solutions. These frequency ranges consisting of unstable periodic solutions or featuring the alternate stable and unstable solutions lead to chaotic responses [45]. Therefore, the whole second passband becomes a chaotic band under a strongly nonlinear state of NAMs. Furthermore, increasing the driving force decreases the generalized amplitude,  $s/F$ , significantly. Accordingly, the stronger nonlinearity results in greater transmission losses in the chaotic band.

These analyses of periodic solutions confirm that the passband between the bridging coupling pair NLR1-NLR2 is a chaotic band that suppresses wave transmissions.

### IV. CONCLUSIONS

The chaotic band in a nonlinear acoustic metamaterial enables ultralow frequency, ultrabroadband, and highly efficient wave reductions (the double-ultra effect) [46]. This work reports the remote bridging coupling of NLR band gaps for efficient manipulations of the chaotic bands.

The triatomic NAM model, whose cell contains two nonlinearly coupled resonators, is created to study the

couplings of NLR band gaps. The properties of nonlinear resonances and nonlinear effective mass are reported, and their relations are clarified by bifurcation analyses in different regimes. This coupling greatly changes the nonlinear effective mass density and features broadband sharing of the negative mass through energy transfer between resonators. For the finite chain, we find numerically that the passband between two NLR band gaps becomes a chaotic band, and increasing the frequency distance between the two NLR band gaps can enhance the efficiency while expanding the bandwidth for wave suppression in the chaotic band. Moreover, the size of NAM does not notably change the modulating principle. This remote interaction is essentially different from the adjacent band gap couplings, so it is called as bridging coupling.

To demonstrate the bridging coupling of NLR band gaps, two NAM beams with different NLR band gap distances are fabricated. We experimentally verify that the transmission losses and the bandwidth of the chaotic band (between and near NLR band gaps) can be modulated by the distance between NLR band gaps. Ultralow frequency and ultrabroadband wave suppressions/attenuations are achieved again (the generalized bandwidth  $\gamma > 15.6$ ). With the nonlinear FE model of the NAM beam, periodic solutions found by the continuation approach confirm that the broadband responses become chaotic waves whose transmissions are amplitude dependent. Therefore, bridging couplings of NLR band gaps are demonstrated to be an efficient mechanism for manipulating the chaotic band in conditions of limited nonlinear strength in practice.

The double-ultra wave suppressions enabled by chaotic bands in NAMs are desired in wide applications, such as vibration and noise control and broadband metadevices. This work reports and demonstrates the remote bridging coupling of nonlinear resonant band gaps for generating and manipulating the chaotic band conveniently and efficiently. Our study extends the content of NAMs and more nonlinear effects are anticipated based on this mechanism.

### ACKNOWLEDGMENTS

This research was funded by the National Natural Science Foundation of China (Projects No.51405502 and No. 51275519).

### APPENDIX: NONLINEAR FINITE ELEMENT MODEL

The modal superposition method is adopted to model the flexural vibration of the oscillators. The first two modes of oscillator 1 and the first mode of oscillator 2 are considered. Transverse displacements,  $w_1(x)$  and  $w_2(x)$ , of oscillator 1 and oscillator 2 are, respectively, expressed by

$$\begin{aligned} w_1(x) &= W_{11}(x)q_{11}(t) + W_{12}(x)q_{12}(t), \\ w_2(x) &= W_{21}(x)q_{21}(t). \end{aligned} \quad (\text{A1})$$

Herein,  $x$  denotes the distance to the fixed point;  $q_{ij}$  is the modal coordinate;  $W_{ij}(x)$  represents the modal displacement given by

$$W_{ij}(x) = \sin \beta_{ij}x - \sinh \beta_{ij}x + \frac{\cos \beta_{ij}L_i + \cosh \beta_{ij}L_i}{\sin \beta_{ij}L_i - \sinh \beta_{ij}L_i} \times (\cos \beta_{ij}x - \cosh \beta_{ij}x), \quad (\text{A2})$$

where  $\cos \beta_{ij}L_i \cosh \beta_{ij}L_i = -1$ . Therefore,  $\beta_{i1}L_i = 1.875$  and  $\beta_{i2}L_i = 4.694$ . The kinetic energy,  $T_r$ , and the strain energy,  $U_r$ , of oscillators in a cell are given by

$$\begin{aligned} T_r = & \frac{1}{2}m_0\dot{w}_0^2 + \frac{1}{2}J_0\dot{\theta}_0^2 + \frac{1}{2}\int_0^{L_1}\rho_1A_1(\dot{w}_0 + \dot{w}_1 + x\dot{\theta}_0)^2 dx \\ & + \frac{1}{2}m_{r1}[\dot{w}_0 + \dot{w}_1(L_1) + L_1\dot{\theta}_0]^2 + \frac{1}{2}J_{r1}[\dot{\theta}_0 + \dot{\theta}_1(L_1)]^2 \\ & + \frac{1}{2}\int_0^{L_2}\rho_2A_2(\dot{w}_0 + \dot{w}_2 + x\dot{\theta}_0)^2 dx \\ & + \frac{1}{2}J_{r2}[\dot{\theta}_0 + \dot{\theta}_2(L_2)]^2 \\ & + \frac{1}{2}m_{r2}[\dot{w}_0 + \dot{w}_2(L_2) + L_2\dot{\theta}_0]^2, \end{aligned} \quad (\text{A3})$$

$$\begin{aligned} U_r = & \frac{1}{2}\int_0^{L_1}E_1I_1(w_{1,xx})^2 dx + \frac{1}{2}\int_0^{L_2}E_2I_2(w_{2,xx})^2 dx \\ & + \frac{1}{2}k_1\Delta^2 + \frac{1}{4}k_n\Delta^4, \\ \Delta = & w_1(L_1, t) - w_2(L_2, t), \quad \theta_i = \partial w_i / \partial x, \end{aligned} \quad (\text{A4})$$

where  $(\cdot)_x = \partial/\partial x$  and  $\dot{X} = \partial X/\partial t$ ;  $w_0$  and  $\theta_0$  are the deflection and angle displacements, respectively, of the primary beam at the fixed point. All parameters are listed in Table I. By substituting Eq. (A2) into Eqs. (A3) and (A4), we obtain

$$T_r = \frac{1}{2}\ddot{\mathbf{q}}_r \tilde{\mathbf{m}}_r \ddot{\mathbf{q}}_r^T, \quad U_r = \frac{1}{2}\tilde{\mathbf{q}}_r \tilde{\mathbf{k}}_{rL} \tilde{\mathbf{q}}_r^T + \frac{1}{4}k_n\Delta^4 \quad (\text{A5})$$

Here, the vector  $\tilde{\mathbf{q}}_r = [w_0 \theta_0 q_{11} q_{12} q_{21}]^T$ ;  $\tilde{\mathbf{m}}_r$  and  $\tilde{\mathbf{k}}_{rL}$  are linear mass and stiffness matrices, respectively. The derivation yields

$$\begin{aligned} \tilde{\mathbf{m}}_r = & \begin{bmatrix} m_{r,11} & m_{r,12} & m_{r,13} & m_{r,14} & m_{r,15} \\ & m_{r,22} & m_{r,23} & m_{r,24} & m_{r,25} \\ & & m_{r,33} & m_{r,34} & 0 \\ & \text{sym} & & m_{r,44} & 0 \\ & & & & m_{r,55} \end{bmatrix}, \\ \tilde{\mathbf{k}}_{rL} = & \begin{bmatrix} 0 & 0 & 0 & 0 & 0 \\ & 0 & 0 & 0 & 0 \\ & & k_{r,33} & k_{r,34} & k_{r,35} \\ & \text{sym} & & k_{r,44} & k_{r,45} \\ & & & & k_{r,55} \end{bmatrix}. \end{aligned} \quad (\text{A6})$$

Elements in  $\tilde{\mathbf{m}}_r$  and  $\tilde{\mathbf{k}}_{rL}$  are not repeated here. The nonlinear term in Eq. (A5) can be simplified by using the formula

$$\Delta = W_{11}(L_1)q_{11} + W_{12}(L_1)q_{12} - W_{21}(L_2)q_{21} + (L_1 - L_2)\theta_0 = q_d. \quad (\text{A7})$$

A transformation yields

$$q_{21} = \frac{(L_1 - L_2)\theta_0 + W_{11}(L_1)q_{11} + W_{12}(L_1)q_{12} - q_d}{W_{21}(L_2)} \quad (\text{A8})$$

Defining a new vector  $\mathbf{q}_r = [w_0 \theta_0 q_{11} q_{12} q_d]^T$ , we obtain  $\tilde{\mathbf{q}}_r = \mathbf{A}_r \mathbf{q}_r$  and

$$\mathbf{A}_r = \begin{bmatrix} 1 & & & & \\ 0 & 1 & & & \\ 0 & 0 & 1 & 0 & 0 \\ 0 & 0 & 0 & 1 & 0 \\ 0 & \frac{L_1-L_2}{W_{21}(L_2)} & \frac{W_{11}(L_1)}{W_{21}(L_2)} & \frac{W_{12}(L_1)}{W_{21}(L_2)} & \frac{-1}{W_{21}(L_2)} \end{bmatrix} \quad (\text{A9})$$

With a vector transformation, the matrices for the mass, the linear stiffness, and the nonlinear stiffness coefficient are

$$\begin{aligned} \mathbf{m}_r &= \mathbf{A}_r^T \tilde{\mathbf{m}}_r \mathbf{A}_r, \\ \mathbf{k}_{rL} &= \mathbf{A}_r^T \tilde{\mathbf{k}}_{rL} \mathbf{A}_r, \\ \mathbf{k}_{rN} &= \mathbf{0} \quad \text{and} \quad k_{rN,55} = k_n. \end{aligned} \quad (\text{A10})$$

If the dissipation arising from the rubber pyramid is approximated as the linear viscous damping, the virtual work done by it is

$$\delta W_d = -c\dot{\Delta}\delta\Delta = -c\dot{q}_d\delta q_d. \quad (\text{A11})$$

Therefore, the motion equation of the oscillators in a cell is expressed as

$$\mathbf{m}_r \ddot{\mathbf{q}}_r + \mathbf{c}_r \dot{\mathbf{q}}_r + \mathbf{k}_{rL} \mathbf{q}_r + \mathbf{k}_{rN} \mathbf{q}_r^3 = \mathbf{f}, \quad (\text{A12})$$

where  $\mathbf{c}_r$  is the damping matrix of the oscillators, and only the element  $c_{r,55} = c$  is nonzero.

As verified, the geometrical nonlinearity of the primary beam is negligible [46]. Furthermore, we establish the FE model of the whole NAM beam by following a standard FE procedure. The motion equation of the whole NAM beam is given by

$$\mathbf{M}\ddot{\mathbf{q}} + \mathbf{K}\mathbf{q} + \mathbf{C}\dot{\mathbf{q}} + \mathbf{N}\mathbf{q}^3 = \mathbf{F} \sin \omega t, \quad (\text{A13})$$

where  $\mathbf{q}$  and  $\mathbf{F}$  are vectors for all nodes' displacement and force, respectively;  $\omega$  denotes the driving frequency at point E;  $\mathbf{M}$ ,  $\mathbf{K}$ ,  $\mathbf{C}$ ,  $\mathbf{N}$  are the system's mass,

linear stiffness, damping, and nonlinear stiffness coefficient matrices, respectively. Besides the damping from the rubber pyramid, the weak dissipation arising from the deformation of the structure is also considered, so matrix  $\mathbf{C}$  is superposed by two damping sources,

$$\mathbf{C} = \mathbf{C}_r + \eta_s \mathbf{K}/\omega. \quad (\text{A14})$$

Here,  $\mathbf{C}_r$  is expanded with the damping matrix  $\mathbf{c}_r$  in Eq. (A12);  $\eta_s$  symbolizes the damping coefficient of the structure. In theoretical analyses, we specify  $c = 0.01$  and  $\eta_s = 1 \times 10^{-5}$ .

The harmonic average approach is adopted to solve the approximate frequency responses (the periodic solutions)

of Eq. (A13) and to determine the stabilities of the solutions. The steps of this algorithm are detailed in Ref. [45]. By defining

$$\mathbf{q} = \mathbf{u} \cos \omega t + \mathbf{v} \sin \omega t, \quad (\text{A15})$$

the periodic solution is determined by the algebraic equations below:

$$\begin{cases} (\mathbf{K} - \omega^2 \mathbf{M})\mathbf{v} - \omega \mathbf{C}\mathbf{u} + 3\mathbf{N}((\mathbf{v}^2 + \mathbf{u}^2)\mathbf{v})/4 = 0, \\ (\mathbf{K} - \omega^2 \mathbf{M})\mathbf{u} + \omega \mathbf{C}\mathbf{v} + 3\mathbf{N}((\mathbf{v}^2 + \mathbf{u}^2)\mathbf{u})/4 = \mathbf{F}. \end{cases} \quad (\text{A16})$$

The Jacobian matrix  $\mathbf{J}$  used to analyze the stabilities of the solutions is given by

$$\mathbf{J} = \begin{bmatrix} \mathbf{M}^{-1} & \mathbf{0} \\ \mathbf{0} & -\mathbf{M}^{-1} \end{bmatrix} \begin{bmatrix} -\omega \mathbf{C} + 3\mathbf{N} \circ [[\mathbf{u}\mathbf{v}]]/2 & \mathbf{K} - \omega^2 \mathbf{M} + 3\mathbf{N} \circ [[3\mathbf{v}^2 + \mathbf{u}^2]]/4 \\ \mathbf{K} - \omega^2 \mathbf{M} + 3\mathbf{N} \circ [[3\mathbf{u}^2 + \mathbf{v}^2]]/4 & \omega \mathbf{C} + 3\mathbf{N} \circ [[\mathbf{u}\mathbf{v}]]/2 \end{bmatrix} \quad (\text{A17})$$

Here,  $\{[\mathbf{x}]\} = [\mathbf{x} \ \mathbf{x} \ \cdots \ \mathbf{x}]^T$  is the algebraic evaluation for expanding a vector  $\mathbf{x}$  into a square matrix  $\{[\mathbf{x}]\}$ .  $\mathbf{A} \circ \mathbf{B} = [a_{ij} b_{ij}]$  is defined as the element product of two matrices  $\mathbf{A}$  and  $\mathbf{B}$ .

Moreover, the perturbation continuation algorithm is adopted to find the convergent solutions of Eq. (A16). Substituting a solution into Eq. (A17) leads to matrix  $\mathbf{J}$ . If there are eigenvalues of  $\mathbf{J}$  having positive real parts, the corresponding solution is unstable; otherwise, it is stable. Due to the inevitable numerical errors, we use a positive value  $\mu_c = 1 \times 10^{-8}$  instead of  $\mu_c = 0$  as the critical value for the real parts of eigenvalues to determine the stability.

- 
- [1] G. Ma and P. Sheng, Acoustic metamaterials: From local resonances to broad horizons, *Sci. Adv.* **2**, e1501595 (2016).
  - [2] Z. Liu, X. Zhang, Y. Mao, Y. Y. Zhu, Z. Yang, C. T. Chan, and P. Sheng, Locally resonant sonic materials, *Science* **289**, 1734 (2000).
  - [3] Z. Liu, C. T. Chan, and P. Sheng, Analytic model of phononic crystals with local resonances, *Phys. Rev. B* **71**, 014103 (2005).
  - [4] S. A. Cummer, J. Christensen, and A. Alù, Controlling sound with acoustic metamaterials, *Nat. Rev. Mater.* **1**, 16001 (2016).
  - [5] N. Fang, D. Xi, J. Xu, M. Ambati, W. Srituravanich, C. Sun, and X. Zhang, Ultrasonic metamaterials with negative modulus, *Nat. Mater.* **5**, 452 (2006).
  - [6] J. Li and C. T. Chan, Double-negative acoustic metamaterial, *Phys. Rev. E* **70**, 055602 (2004).
  - [7] V. C. Henriquez, V. M. García-Chocano, and J. Sánchez-Dehesa, Viscothermal Losses in Double-Negative Acoustic Metamaterials, *Phys. Rev. Appl.* **8**, 014029 (2017).

- 
- [8] H. Dong, S. Zhao, Y. Wang, and C. Zhang, Topology optimization of anisotropic broadband double-negative elastic metamaterials, *J. Mech. Phys. Solids* **105**, 54 (2017).
  - [9] V. E. Gusev and O. B. Wright, Double-negative flexural acoustic metamaterial, *New J. Phys.* **16**, 123053 (2014).
  - [10] M. I. Hussein, M. J. Leamy, and M. Ruzzene, Dynamics of phononic materials and structures: Historical origins, recent progress, and future outlook, *Appl. Mech. Rev.* **66**, 040802 (2014).
  - [11] Z. Yang, H. M. Dai, N. H. Chan, G. C. Ma, and P. Sheng, Acoustic metamaterial panels for sound attenuation in the 50–1000 Hz regime, *Appl. Phys. Lett.* **96**, 1833 (2010).
  - [12] Y. Song, L. Feng, J. Wen, D. Yu, and X. Wen, Reduction of the sound transmission of a periodic sandwich plate using the stop band concept, *Compos. Struct.* **128**, 428 (2015).
  - [13] H. Zhang, Y. Xiao, J. Wen, D. Yu, and X. Wen, Flexural wave band gaps in metamaterial beams with membrane-type resonators: Theory and experiment, *J. Phys. D: Appl. Phys.* **48**, 435305 (2015).
  - [14] M. Yang and P. Sheng, Sound absorption structures: From porous media to acoustic metamaterials, *Annu. Rev. Mater. Res.* **47**, 83 (2017).
  - [15] M. Ambati, N. Fang, C. Sun, and X. Zhang, Surface resonant states and superlensing in acoustic metamaterials, *Phys. Rev. B* **75**, 195447 (2007).
  - [16] N. Kaina, F. Lemoult, M. Fink, and G. Lerosey, Negative refractive index and acoustic superlens from multiple scattering in single negative metamaterials, *Nature* **525**, 77 (2015).
  - [17] H. Zhu and F. Semperlotti, Double-Zero-Index Structural Phononic Waveguides, *Phys. Rev. Appl.* **8**, 064031 (2017).
  - [18] Y. Chen, M. Zheng, X. Liu, Y. Bi, Z. Sun, P. Xiang, J. Yang, and G. Hu, Broadband solid cloak for underwater acoustics, *Phys. Rev. B* **95**, 180104 (2017).

- [19] Y. Zhu, X. Fan, B. Liang, J. Cheng, and Y. Jing, Ultrathin Acoustic Metasurface-Based Schroeder Diffuser, *Phys. Rev. X* **7**, 021034 (2017).
- [20] Y. Wang, H. Zhao, H. Yang, J. Zhong, and J. Wen, A space-coiled acoustic metamaterial with tunable low-frequency sound absorption, *Europhys. Lett.* **120**, 54001 (2017).
- [21] Y. Xiao, J. Wen, and X. Wen, Longitudinal wave band gaps in metamaterial-based elastic rods containing multi-degree-of-freedom resonators, *New J. Phys.* **14**, 33042 (2012).
- [22] Y. Xiao, J. Wen, and X. Wen, Flexural wave band gaps in locally resonant thin plates with periodically attached spring-mass resonators, *J. Phys. D: Appl. Phys.* **45**, 195401 (2012).
- [23] P. F. Pai, H. Peng, and S. Jiang, Acoustic metamaterial beams based on multi-frequency vibration absorbers, *Int. J. Mech. Sci.* **79**, 195 (2014).
- [24] V. Romero-García, A. Krynkin, L. M. Garcia-Raffi, O. Umnova, and J. V. Sánchez-Pérez, Multi-resonant scatterers in sonic crystals: Locally multi-resonant acoustic metamaterial, *J. Sound Vibr.* **332**, 184 (2013).
- [25] Y. Xiao, J. Wen, G. Wang, and X. Wen, Theoretical and experimental study of locally resonant and Bragg band gaps in flexural beams carrying periodic arrays of beam-like resonators, *J. Vib. Acoust.* **135**, 041006 (2013).
- [26] E. G. Williams, P. Roux, M. Rupin, and W. A. Kuperman, Theory of multiresonant metamaterials for A0 Lamb waves, *Phys. Rev. B* **91**, 104307 (2015).
- [27] A. Poincaré, *The Fermi-Pasta-Ulam Problem in the Thermodynamic Limit* (Springer, Netherlands, 2005), pp. 431–440.
- [28] S. Flach and A. Poincaré, The Fermi–Pasta–Ulam problem: Periodic orbits, normal forms and resonance overlap criteria, *Physica D* **237**, 908 (2008).
- [29] V. F. Nesterenko, C. Daraio, E. B. Herbold, and S. Jin, Anomalous Wave Reflection at the Interface of Two Strongly Nonlinear Granular Media, *Phys. Rev. Lett.* **95**, 158702 (2005).
- [30] C. Daraio, V. F. Nesterenko, E. B. Herbold, and S. Jin, Tunability of solitary wave properties in one-dimensional strongly nonlinear phononic crystals, *Phys. Rev. E* **73**, 026610 (2006).
- [31] R. K. Narisetti, M. J. Leamy, and M. Ruzzene, A perturbation approach for predicting wave propagation in one-dimensional nonlinear periodic structures, *J. Vib. Acoust.* **132**, 031001-1-031001-11 (2010).
- [32] N. Boechler, G. Theoharis, and C. Daraio, Bifurcation-based acoustic switching and rectification, *Nat. Mater.* **10**, 665 (2011).
- [33] B. Liang, X. S. Guo, J. Tu, D. Zhang, and J. C. Cheng, An acoustic rectifier, *Nat. Mater.* **9**, 989 (2010).
- [34] N. I. Zheludev and Y. S. Kivshar, From metamaterials to metadevices, *Nat. Mater.* **11**, 917 (2012).
- [35] M. Kauranen and A. V. Zayats, Nonlinear plasmonics, *Nat. Photonics* **6**, 737 (2012).
- [36] M. Lapine, New degrees of freedom in nonlinear metamaterials, *Phys. Status Solidi B* **254**, 1600462 (2017).
- [37] K. Yang, R. Verre, J. Butet, C. Yan, T. J. Antosiewicz, M. Käll, and O. J. F. Martin, Wavevector-selective nonlinear plasmonic metasurfaces, *Nano Lett.* **17**, 5258 (2017).
- [38] L. Fan, H. Ge, S. Y. Zhang, H. F. Gao, Y. H. Liu, and H. Zhang, Nonlinear acoustic fields in acoustic metamaterial based on a cylindrical pipe with periodically arranged side holes, *J. Acoust. Soc. Am.* **133**, 3846 (2013).
- [39] N. Sugimoto, Propagation of nonlinear acoustic waves in a tunnel with an array of Helmholtz resonators, *J. Fluid Mech.* **244**, 55 (1992).
- [40] N. Sugimoto, Acoustic solitary waves in a tunnel with an array of Helmholtz resonators, *J. Acoust. Soc. Am.* **99**, 1971 (1996).
- [41] Y. Li, J. Lan, B. Li, X. Liu, and J. Zhang, Nonlinear effects in an acoustic metamaterial with simultaneous negative modulus and density, *J. Appl. Phys.* **120**, 145105 (2016).
- [42] J. Lan, Y. Li, H. Yu, B. Li, and X. Liu, Nonlinear effects in acoustic metamaterial based on a cylindrical pipe with ordered Helmholtz resonators, *Phys. Lett. A* **381**, 1111 (2017).
- [43] X. Fang, J. Wen, J. Yin, D. Yu, and Y. Xiao, Broadband and tunable one-dimensional strongly nonlinear acoustic metamaterials: Theoretical study, *Phys. Rev. E* **94**, 052206 (2016).
- [44] X. Fang, J. Wen, J. Yin, and D. Yu, Wave propagation in nonlinear metamaterial multi-atomic chains based on homotopy method, *AIP Adv.* **6**, 121706 (2016).
- [45] X. Fang, J. Wen, B. Bonello, J. Yin, and D. Yu, Wave propagation in one-dimensional nonlinear acoustic metamaterials, *New J. Phys.* **19**, 053007 (2017).
- [46] X. Fang, J. Wen, B. Bonello, J. Yin, and D. Yu, Ultra-low and ultra-broad-band nonlinear acoustic metamaterials, *Nat. Commun.* **8**, 1288 (2017).
- [47] X. Fang, J. Wen, D. Yu, and G. Huang, Wave propagation in infinite nonlinear acoustic metamaterial beam by considering the third harmonic generation, arXiv:1808.04682.